

RE-EXAMINATION OF THE EXPECTED GAMMA-RAY EMISSION OF SUPERNOVA REMNANT SN 1987A

E.G. BEREZHKO¹, L.T. KSENOFONTOV¹, AND H.J. VÖLK²
Draft version February 23, 2019

ABSTRACT

A nonlinear kinetic theory, combining cosmic ray (CR) acceleration in supernova remnants (SNRs) with their gas dynamics, is used to re-examine the nonthermal properties of the remnant of SN 1987A for an extended evolutionary period of 5-50 yr. This spherically symmetric model is approximately applied to the different features of the SNR which consist of (i) a blue supergiant wind and bubble, and (ii) of the swept-up red supergiant (RSG) wind structures in the form of an HII region, an equatorial ring (ER), and an hourglass region. The RSG wind involves a mass loss rate that decreases significantly with elevation above and below the equatorial plane. The model adapts recent three-dimensional hydrodynamical simulations by Potter et al. (2014) which use a significantly smaller ionized mass of the ER than assumed in the earlier studies by the present authors. The SNR shock has recently swept up the ER which is the densest region in the immediate circumstellar environment. Therefore the expected gamma-ray energy flux density at TeV-energies at the current epoch has already reached its maximal value $\sim 10^{-13}$ erg cm⁻²s⁻¹. This flux should decrease by a factor of about two over the next ten years.

Subject headings: acceleration of particles — ISM: individual objects (SN 1987A) — ISM: supernova remnants — X-rays: individual (SN 1987A) — gamma rays: ISM

1. INTRODUCTION

The Supernova (SN) which occurred in 1987 in the nearby Large Magellanic Cloud was the first object of its kind whose evolution in the radio to the X-ray range has been resolved as a function of time. The study of SN 1987A continues and includes in particular extensive observations in Very High Energy (VHE; $E > 100$ GeV) γ -rays (e.g. H.E.S.S. Collaboration 2015).

The present work is a critical re-examination and extension of the studies by Berezhko & Ksenofontov (2000, 2006) and Berezhko et al. (2011)(referred to as BKV11 in the following), concerning the properties of the non-thermal emission of SN 1987A. As in those previous investigations the framework is a nonlinear kinetic theory of cosmic ray (CR) acceleration in supernova remnants (SNRs). It couples the particle acceleration process with the hydrodynamics of the thermal gas (Berezhko et al. 1996), and connects it with the gamma-ray emission (e.g. Berezhko & Völk 2000). The application of this theory to individual SNRs (see Völk 2004; Berezhko 2005, 2008, 2014, for reviews) has demonstrated its capability to explain the observed SNR properties and radiation spectra. Combining the theoretical model with the *observed* synchrotron spectra predicts new effects like the large degree of magnetic field amplification that leads to the observed concentration of the highest-energy electrons in a very thin shell just behind the forward shock into the circumstellar medium (CSM).

The evolution of the radio and X-ray emission at earlier times, implied also in the present paper, has been described by e.g. BKV11 who showed in particular that the evidence for strong shock modification comes primar-

ily from radio data.

Efficient acceleration of the CR proton component is needed to produce significant shock modification leading to a soft and concave CR electron spectrum in SN 1987A which fits very well the observed nonthermal radio emission and X-ray spectra, if the downstream magnetic field strength B_d is as high as ≈ 15 mG. Such a high field leads to significant electron synchrotron losses that cut off the high frequency X-ray part of the synchrotron spectrum, consistent with the X-ray observations. The required magnetic field strength is presumably to be attributed to its nonlinear amplification near the SNR shock by the CR acceleration process itself (Bell 2004).

As a consequence of the efficient production of the CR nuclear component, that is accompanied by strong magnetic field amplification, SN 1987A is expected to be a potential source of γ -rays for the H.E.S.S. instrument. However the flux of TeV-emission predicted in BKV11 exceeds the upper limit obtained by H.E.S.S. (H.E.S.S. Collaboration 2015). It is suggested here that this inconsistency is the result of an overestimate of the CSM gas density, in particular of the mass of the equatorial ring (ER).

The present work uses the same canonical values (e.g. McCray 1993) for the stellar ejecta mass M_{ej} , distance d , hydrodynamic explosion energy E_{sn} and ejecta velocity distribution as BKV11, but takes account of the detailed radio continuum observations by Ng et al. (2013) and Zanardo et al. (2014). In particular, it makes use of the recent, extensive CSM modeling in terms of three-dimensional hydrodynamical simulations by Potter et al. (2014) (in the sequel referred to as Potter14). An approximate prediction of the future nonthermal emission from SN 1987A for the next decades is given. The densest part of the CSM, which lies within the range $|\theta| < 20^\circ$ of the elevation angle θ around the equatorial plane, is then considerably less dense than what was adopted in

ksenofon@ikfia.sbras.ru

¹ Yu.G. Shafer Institute of Cosmophysical Research and Aeronomy, 31 Lenin Ave., 677980 Yakutsk, Russia

² Max Planck Institut für Kernphysik, Postfach 103980, D-69029 Heidelberg, Germany

BKV11. This is the main reason for the re-examination of the CR production in SN 1987A and the associated nonthermal emission.

2. SN 1987A AND ITS CIRCUMSTELLAR ENVIRONMENT

To study the propagation of the SN shock through the CSM the results of Potter14 for the angular range $|\theta| < 20^\circ$ relative to the equatorial plane are used³. The most efficient CR and nonthermal emission production presumably takes place within this region. This is roughly consistent with the radio observations (Ng et al. 2013). The adopted radial profile of gas number density $N_g = \rho/m_p$ in this region is represented in Figure 1. Within the selected elevation range it consists of several different morphological structures: (i) the wind bubble of the blue supergiant (BSG) progenitor star (Chevalier & Fransson 1987) at $r < R_C = 4.5 \times 10^{17}$ cm with gas density $N_g = 0.29 \text{ cm}^{-3}$ (ii) the HII region (Chevalier & Dwarkadas 1995) at $R_C < r < R_{\text{HG}} = 8 \times 10^{17}$ cm with $N_g = 280 \text{ cm}^{-3}$ (iii) the so-called hourglass region at $R_{\text{HG}} < r < R_W = 1.5 \times 10^{18}$ cm with $N_g = 10 \text{ cm}^{-3}$, and (iv) the free red supergiant (RSG) wind region at $R > R_W$ with $N_g = 10(r/R_W)^3 \text{ cm}^{-3}$; the properties of the structures (iii) and (iv) follow directly from Potter14. Within the smaller elevation angle region of $|\theta| < 4.5^\circ$ the same radial profile includes the equatorial ring, inside the HII region (see Figure 1). Its gas number density is chosen here to be distributed according to the relation

$$N_g = N_{\text{gm}} \exp[-(r - R_{\text{ER}})^2/l_{\text{ER}}^2], \quad (1)$$

where $N_{\text{gm}} \approx M_{\text{sh}}/(4\pi^{3/2}m_p R_{\text{ER}}^2 l_{\text{ER}})$ is the central (maximal) density of the ER; M_{ER} , R_{ER} and l_{ER} denote the total mass, the radius and the width of the ER, respectively. Below, the values $M_{\text{ER}} = 0.058M_\odot$, $R_{\text{ER}} = 6.4 \times 10^{17}$ cm and $l_{\text{ER}} = 0.12R_{\text{ER}}$ are used. These parameter values are taken in order to fit the observed shock and radio-emission dynamics. They turn out to be consistent with the values used by Potter14.

The CSM, described above, differs significantly from the CSM adopted in BKV11. First of all, the ER mass, albeit that of the ionized material only, $M_{\text{ER}} = 0.058M_\odot$ (Mattila et al. 2010), is considerably smaller than used by BKV11 ($M_{\text{ER}} = 0.5M_\odot$). Secondly, the CSM behind the ER is less dense. These factors, as demonstrated below, lead to a considerable reduction of the expected nonthermal emission, in particular of the γ -ray emission, compared with the results of BKV11.

3. PARTICLE ACCELERATION MODEL

3.1. Shock approximation

The propagation of the forward SN shock through the CSM is modeled in the spirit of a spherically symmetrical approach. It approximates the shock and its effects as the weighted sum of two independent spherically symmetric shocks, propagating into, respectively, two different radial gas number density profiles of the CSM, shown in Figure 1: the first profile (region 1) belongs to an azimuthally symmetric region of elevation angles θ near

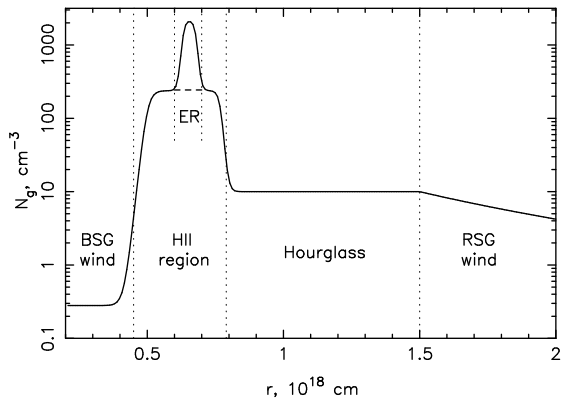


FIG. 1.— Radial profiles of CSM gas density N_g . The partly overlapping thick dashed and solid lines respectively correspond to region 1 ($4.5^\circ < |\theta| < 20^\circ$) and region 2 ($|\theta| < 4.5^\circ$) in elevation angle θ . The radial extent of the various morphological structures, summarized in section 2, is indicated by the vertical dotted lines.

the equatorial plane $4.5^\circ < |\theta| < 20^\circ$, and the second, analogous profile (region 2), corresponds to the innermost $|\theta| < 4.5^\circ$. Then each quantity Q , characterizing the number of accelerated CRs and the amount of the emission produced by these CRs, is determined by the relation

$$Q = Q_1(f_1 - f_2) + Q_2 f_2, \quad (2)$$

where $Q_{1,2}$ are the spherically symmetric values corresponding to the profiles that characterize the two regions 1 and 2, respectively, and $f_1 = 0.34$ and $f_2 = 0.08$ denote the filling factors in solid angle of these regions.

CR production by the SN shock at high latitudes $|\theta| > 20^\circ$ is neglected here because the gas density in this region is considerably lower (see Potter14). We also neglect CR production at the reverse shock for the reasons given in BKV11.

The question is of course, to what extent such an approximate treatment remains consistent as a function of time, with the real SNR shock sweeping across the real CSM to reach larger and larger radial distances. A priori the decrease of the gas density with elevation angle, symmetric to the equatorial plane, suggests this to be roughly stable process. However, effects like the engulfment of the ER clearly imply some non-radial shock propagation aspects. They are also apparent in the three-dimensional simulations of Potter14. In addition, the ring is clumpy, even though Fransson et al. (2015) found indications that these hot spots are now gradually dissolving. This type of effects should influence primarily the detailed time dependence of the particle acceleration and hadronic γ -ray emission rather than the global acceleration properties of the system⁴. Therefore, in a gross sense, the used mosaic of spherical shocks appears as an adequate overall approximation.

3.2. Field amplification, injection rate, electron to proton ratio

As in BKV11 the magnetic field strength B_0 , given by the expression

$$B_0 = \sqrt{2\pi \times 10^{-2} \rho_0 V_s^2} \quad (3)$$

³ The equatorial-to-polar density ratio is 20:1 (Blondin & Lundqvist 1993)

⁴ For discussions of such effects, see however Berezhko et al. (2013); Gabici & Aharonian (2014).

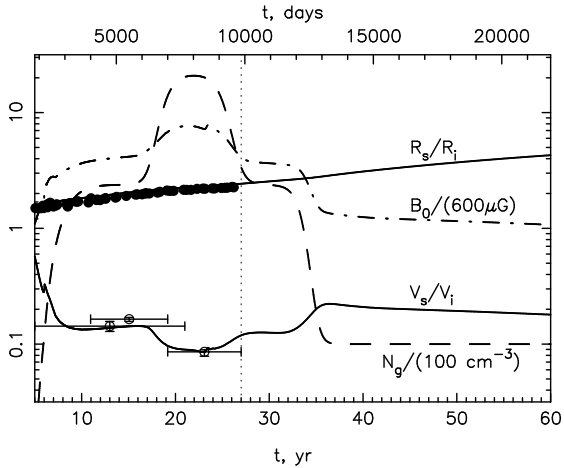


FIG. 2.— Shock radius R_s and shock speed V_s (solid lines), gas number density N_g (dash-dotted line) and upstream magnetic field B_0 (dashed line) at the current shock position as a function of time since SN explosion, for region 2. The dotted vertical line marks the current epoch. The observed radius R_s and speed V_s of the SN shock, as determined by radio observations (Ng et al. 2013) are shown as well. The scaling values are $R_i = R_T = 3.1 \times 10^{17}$ cm and $V_i = 28000$ km s $^{-1}$

is used. Here V_s denotes the SN shock speed and B_0 is the far upstream field, presumably amplified by the CRs of the highest energy. In the same sense ρ_0 is the far upstream mass density. The high downstream magnetic field $B_d = B_0 \times \sigma \approx 10$ mG, where σ denotes the total shock compression ratio, is required to reproduce the observed radio and X-ray spectra (Berezhko & Ksenofontov 2006). The calculation of the shock radius R_s and speed V_s again follows the scheme of (Berezhko & Ksenofontov 2006), see also BKV11, as does the evaluation of the proton injection rate ηN_g and of the electron to proton ratio K_{ep} .

4. RESULTS AND DISCUSSION

Figure 2 shows R_s and V_s , as the shock propagates in the CSM corresponding to region 2, together with the latest radio data (Ng et al. 2013). In the case of region 1 the shock speed time profile $V_s(t)$ does not contain the local minimum around $t = 8000$ d; this is the main difference to the results presented in Figure 2. Iteratively fitting the theoretical quantities $\eta(t)$ and $K_{ep}(t)$ to the spatially-integrated radio synchrotron spectra up to the year 2013 (Ng et al. 2013), leads to a constant value for $K_{ep}(t) = 3 \times 10^{-3}$, whereas the value $\eta(t) \approx 3 \times 10^{-3}$ at $t \approx 26$ yr (Figure 3a) is due to the assumption that, leaving the HII region, the nuclear injection fraction should go back, after $t \approx 30$ yr to its value before the age of 10 years. During the ages between about 10 yr and 30 yr the compressed and largely azimuthal magnetic field of the HII region should have depressed nuclear injection, consistent with the softening of the spatially-integrated radio spectrum (with index $\alpha(t)$) as shown in Figure 3b. This Figure also shows that outside the HII region the shock is significantly modified relative to a pure gas shock for which the total shock compression ratio σ and the subshock compression ratio σ_s would both have a value of 4.

The adopted value of $\eta(t)$ determines the amount of shock modification, in particular the decrease of the subshock compression ratio $\sigma_s(t)$ relative its value of 4 for

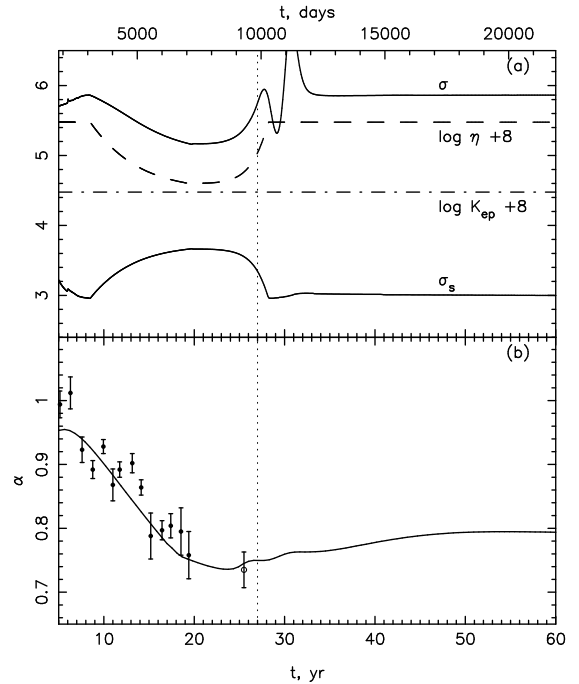


FIG. 3.— (a) Shock compression ratio σ and subshock compression ratio σ_s (solid lines), proton injection fraction η (dashed line), and electron-to-proton ratio dK_{ep} (dash-dotted line) as functions of time. (b) Selfconsistent spectral index α of the integrated nonthermal radio emission as a function of time together with observational data from ATCA (Zanardo et al. 2010) and the latest combination of ATCA and ALMA (Zanardo et al. 2014).

an unmodified shock. Since CRs with relatively small energies are produced near the subshock, the value $\sigma_s(t)$ directly determines the shape of the electron energy spectrum at energies below ≈ 1 GeV - which produce synchrotron emission in the radio range - and vice versa. Therefore, as in all similar cases, the proton injection rate $\eta(t)$ is inferred from a fit of the resulting theoretical spectral index $\alpha(t)$ of the integrated radio synchrotron emission to the observed value. The quality of this fit can be ascertained from Figure 3b, where the best calculated time profile $\alpha(t)$ is presented together with the observational data.

From the epoch $t > 6$ yr onwards the value $\alpha(t)$ decreases up to the epoch $t \approx 23$ yr (Zanardo et al. 2010) and is assumed to start to increase again at $t > 23$ yr. This appears to be consistent with recent measurements by Indebetouw et al. (2014) and, especially, Zanardo et al. (2014). However, the increase is not as fast as one would expect from the behavior of the local $\sigma_s(t)$. This occurs because at subsequent epochs the gas number density and consequently also the amount of freshly injected electrons, as well as the magnetic field strength, are much smaller than when the shock was in the HII region. Therefore the synchrotron emission of those latter electrons, convected downstream in that higher magnetic field remains dominant. For similar reasons the variation in the shock compression ratio σ at an age 10000–12000 days, caused by the rapid decrease of the upstream gas number density N_g , does not significantly affect the integrated radio synchrotron emission flux, and the spectral index α remains essentially independent of σ .

Using these educated guesses for η and K_{ep} the calcu-

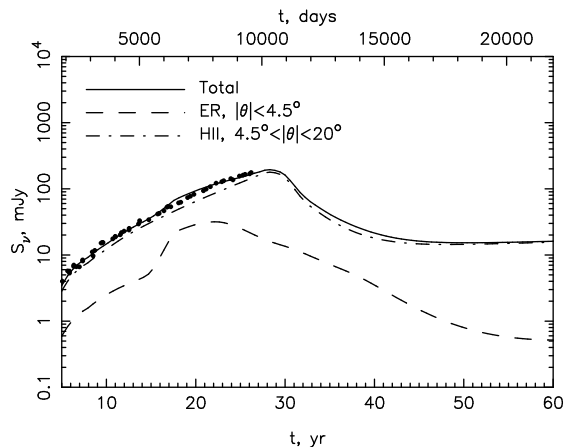


FIG. 4.— Calculated flux of radio emission at frequency $\nu = 9$ GHz as a function of time, together with the ATCA data (Ng et al. 2013). Dashed and solid lines represent the contribution of region 1 and of the sum from regions 1 and 2, respectively.

lated flux of radio emission S_ν at frequency $\nu = 9$ GHz is presented in Figure 4 together with the observational data obtained with the ATCA instrument (Ng et al. 2013). For those times where the radio flux has also been measured the calculation is perfectly consistent with the observations. According to the calculation the rapid growth of radio emission in the epochs $t < 30$ yr is due to the increase of the number of accelerated CR electrons, which is proportional to the swept-up mass within the HII region. For the adopted value of the outer boundary of the HII region, $R_{HG} = 8 \times 10^{17}$ cm, the SNR shock reaches this boundary after $t \approx 30$ yr, and the peak of radio emission is reached. Even at later epochs, $t = 30 - 40$ yrs, the radio synchrotron emission will still be dominated by the contribution of the swept-up matter of the HII region. The flux of radio emission is expected to decrease gradually by a factor of about 10 during 10 years after 2017. Due to its considerably lower gas density the contribution of the swept-up hourglass matter will become essential only for $t > 43$ yr, when the radio emission starts to grow slowly again.

The calculated γ -ray energy flux density above 3 TeV as a function of time, shown in Figure 5, is dominated by the π^0 -decay component at all energies. Since a significant part of the shock surface is expected to be tangential and therefore to not efficiently inject/accelerate nuclear CRs, the overall number of accelerating CRs is normalized by a factor $f_{re} = 0.2$, as argued by Völk et al. (2003) and BKV11 before.

As it is clear from Figure 5, the region 1 which contains the ER, the densest structure, contributes dominantly only during the shock propagation through the ER, that is during the days 7000-10000.

According to Figure 5 the maximal energy flux density of TeV-emission $\epsilon_\gamma F_\gamma \approx 7 \times 10^{-2}$ eV cm $^{-2}$ s $^{-1}$ was achieved at day 9000, and after that epoch it decreased continuously due to the decrease of the CSM gas density. Since the radial gas density profile is much thinner compared with the one used earlier BKV11, the peak value of the expected flux of TeV-emission is now lower and the TeV-emission expected for the future is considerably lower.

The most recent upper limit for the TeV emission

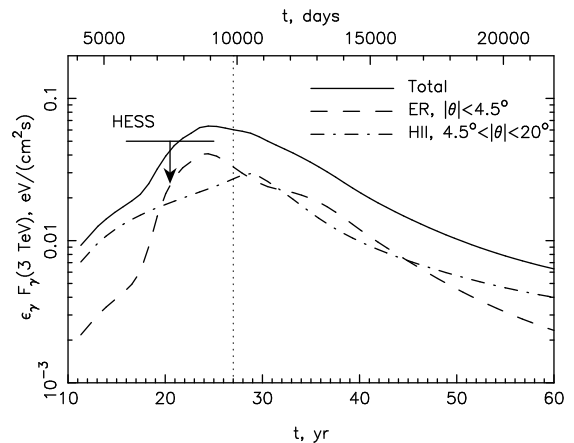


FIG. 5.— Integral γ -ray energy flux density above 3 TeV from SN 1987A as a function of time. The H.E.S.S. (H.E.S.S. Collaboration 2015) upper limit, corresponding to the observational period 2005-2012 yr, is shown as well.

obtained by the H.E.S.S. telescopes during the period 2005-2012 (H.E.S.S. Collaboration 2015) (see Figure 5) is roughly consistent with this prediction.

According to the calculation (see Figure 5) the most promising time for the detection of SN 1987A in TeV γ -rays is the 10-year period from 2008 to 2018. At later epochs SN 1987A should be detectable in the VHE range only by an instrument with a higher sensitivity than that of H.E.S.S.

This work has been supported in part by the Russian Foundation for Basic Research (grants 13-02-00943 and 13-02-12036) and by the Council of the President of the Russian Federation for Support of Young Scientists and Leading Scientific Schools (project No. NSH-3269.2014.2).

5. APPENDIX

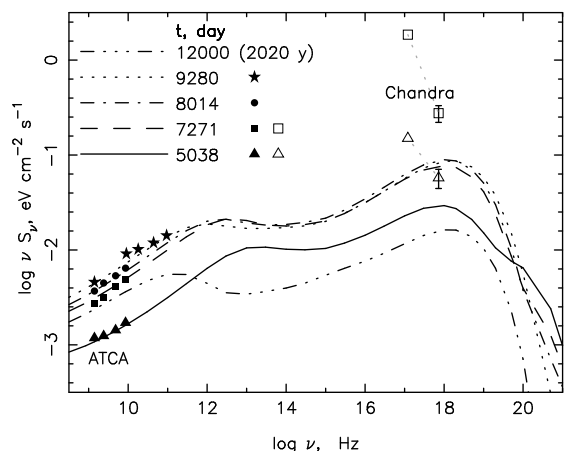


FIG. 6.— Spatially-integrated synchrotron spectral energy flux density of SN 1987A, calculated for five evolutionary epochs. The ATCA radio data (Zanardo et al. 2010, 2014) for four epochs are shown as well, together with the *Chandra* X-ray flux (Park et al. 2007) data for two epochs (both in the soft energy range at $\nu = 10^{17}$ Hz and, connected by dotted lines, in the hard energy range at $\nu = 6 \times 10^{17}$ Hz).

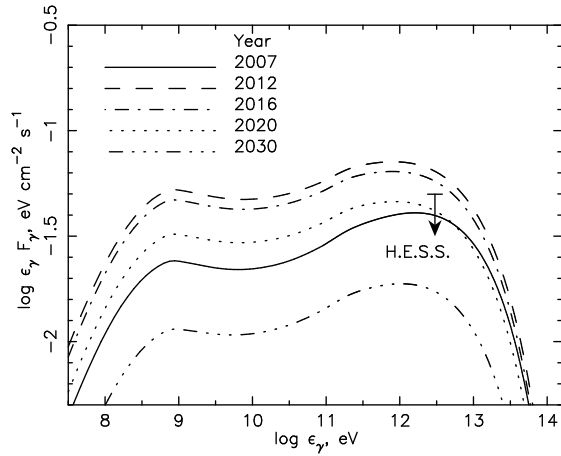


FIG. 7.— Spatially-integrated γ -ray spectral energy flux density, calculated for five epochs. The recent H.E.S.S. upper limit (H.E.S.S. Collaboration 2015) is shown as well.

REFERENCES

- Bell, A.R. 2004, MNRAS, 353, 550
 Berezhko, E. G., Elshin, V. K., & Ksenofontov, L. T. 1996, JETP, 82, 1
 Berezhko, E.G. & Völk, H.J. 2000, A&A, 357, 283
 Berezhko, E. G., & Ksenofontov, L. T. 2000, Astronomy Letters, 26, 639
 Berezhko, E. G., & Ksenofontov, L. T. 2006, ApJ, 650, L59.
 Berezhko, E.G. 2005, Adv. Space Res., 35, 1031
 Berezhko, E.G. 2008, Adv. Space Res., 41, 429
 Berezhko, E.G. 2014, Nuc. Phys. B (Proc. Suppl.), 256, 23
 Berezhko, E.G., Ksenofontov, L.T., & Völk, H.J. 2011, ApJ, 732, 58 (BKV11)
 Berezhko, E.G., Ksenofontov, L.T., & Völk, H.J. 2013, ApJ, 763, 14
 Blondin, J.M., & Lundqvist, P. 1993, ApJ, 405, 337
 Chevalier, R. A. & Dwarkadas, V. V. 1995, ApJ, 452, L45
 Chevalier, R. A., & Fransson, C. 1987, Nature, 328, 44
 Fransson, C., Larsson, J., Migotte, K., et al. 2015, ApJ, 806, L19
 Gabici, S., Aharonian, F.A. 2014, MNRAS, 445, L70
 H.E.S.S. Collaboration. 2015, Science, 347, 406
 Indebetouw, R., Matsuura, M., Dwek, E. et al. 2014, ApJ, 782, L2
 Mattila, S., Lundqvist, P., Gröningson, P., et al. 2010, ApJ, 717, 1140
 McCray, R. 1993, ARA&A, 31 175
 Ng, C.-Y., Zanardo, G., Staveley-Smith, L. et al. 2013, ApJ, 777, 131
 Park, S., Burrows, D. N., Garmire, G. P. et al. 2007, AIP Conf.Proc., 937, 43
 Potter, T.M., Staveley-Smith, L., Reville, B. et al. 2014, ApJ, 794, 174
 Völk, H. J. 2004, Proc. 28th ICRC (Tsukuba), 8, 29
 Völk, H. J., Berezhko, E. G., & Ksenofontov, L. T. 2003, A&A, 409, 563
 Zanardo, G., Staveley-Smith, L., Ball, L., et al. 2010, ApJ, 710, 1515
 Zanardo, G., Staveley-Smith, L., Indebetouw, R., et al. 2014, ApJ, 796, 82